Magnetic field energy dissipation due to particle trapping in a force-free configuration of collisionless pair plasmas

J. I. Sakai,[1] D. Sugiyama,[1] T. Haruki,[1] N. Bobrova,[1,2] and S. Bulanov[1,3]
[1]*Laboratory for Plasma Astrophysics, Faculty of Engineering, Toyama University, Toyama 930-8555, Japan*
[2]*Institute of Experimental and Theoretical Physics, Moscow, Russia*
[3]*General Physics Institute, RAS, Moscow, Russia*

(Received 25 June 2000; revised manuscript received 2 November 2000; published 27 March 2001)

It is shown by using a two-dimensional, fully relativistic, electromagnetic particle-in-cell simulation code that a force-free magnetic configuration in collisionless, electron-positron (pair) plasmas becomes unstable against current-driven Buneman instability and subsequently there occurs a strong magnetic field energy dissipation associated with collisionless magnetic reconnection, which can be driven by particle trapping due to two-dimensional electric potentials remaining in the nonlinear stage of the initial current-driven Buneman instability. About 43% of the initial magnetic field energy dissipates and is transformed to plasma heating as well as high-energy particle production. The energy spectrum in the high-energy region is given by an exponential type with two temperatures. We also show the simulation results for the electron-ion plasma to compare the effect of the mass ratio of the electron and proton.

DOI: 10.1103/PhysRevE.63.046408 PACS number(s): 52.35.−g

I. INTRODUCTION

Magnetic field generation and dissipation in astrophysical plasmas are important processes for understanding physical mechanisms of plasma heating as well as high-energy particle production. Many astrophysical plasmas are collisionless during the period when the interesting physical processes are taking place. In such collisionless plasmas the physical mechanisms causing the magnetic field dissipation through the magnetic reconnection [1] are still under many investigations. Among them collisionless tearing instability [2] was first investigated, which is a dissipation mechanism due to wave-particle resonance (Landau resonance) in a null magnetic field region. Other mechanisms due to some turbulent collisions between small scale waves and current-carrying particles are proposed: for example, lower-hybrid waves [3], drift-kink waves [4], and so on.

Recently a collisionless tearing instability has been investigated [5] in a force-free magnetic configuration in an electron-proton plasma and in the nonlinear stage, strong magnetic field energy dissipation has been observed in a two-dimensional particle-in-cell (PIC) code simulation. Sakai *et al.* [5] suggested that the strong magnetic field dissipation is caused by collisionless magnetic reconnection, which can be driven by electron trapping due to two-dimensional electrostatic potentials.

In the present paper we show by using a fully relativistic PIC simulation code that there occurs very effective magnetic field dissipation through collisionless magnetic reconnection triggered by particle trapping in the quasistatic two-dimensional electric potentials remaining in the late phase of the current-driven instability in pair plasmas. About 43% of the initial magnetic field energy dissipates and is transformed to plasma heating as well as high-energy particle production. We also show the simulation results for the electron-ion plasma, to compare the effect of the mass ratio of the electron and proton. In Sec. II we show our simulation model. In Sec. III we present our simulation results and summarize our results in Sec. IV.

II. SIMULATION MODEL

The simulation code used here is a two-and-a-half-dimensional code, assuming that the physical quantities are constant in z ($\partial/\partial z=0$), which was modified from the three-dimensional, fully electromagnetic, and relativistic TRISTAN code [6]. The system size is $L_x=300\Delta$ and $L_y=80\Delta$, where Δ $(=1)$ is the grid size. Periodic boundary conditions are imposed on particles and fields. There are 2.4×10^6 electron-positron pairs filling the entire domain uniformly, keeping the domain charge neutral. Hence the average particle number density is about 100 per cell.

We consider a simple force-free configuration with current sheets in which magnetic fields are given by

$$B_x(y)=B_0\sin\left(\frac{y-40}{L}\right), \tag{1}$$

$$B_y(y)=0, \tag{2}$$

$$B_z(y)=B_0\cos\left(\frac{y-40}{L}\right), \tag{3}$$

where $L(=40\Delta/\pi)$ is the width of the current sheets. The central lines of the current sheets in the x-y plane are located at $y=0,40,80$. To generate the above magnetic fields, we impose shifted Maxwell distributions with a drift velocity v_d in the x and z directions for both electron and positron velocity distributions. We investigated two cases: (a) $v_d=0.25c=2.65v_{te}$ and (b) $v_d=0.13c=1.38v_{te}$. Here we show mostly the results of the case (a). The initial state is characterized by complete charge neutrality ($\mathbf{E}_0=\mathbf{0}$) everywhere in the domain. Other parameters are as follows: the mass ratio between an electron and a positron, $m_e/m_p=1$; the simulation time step $\omega_{pe}\Delta t=0.052$; the plasma fre-

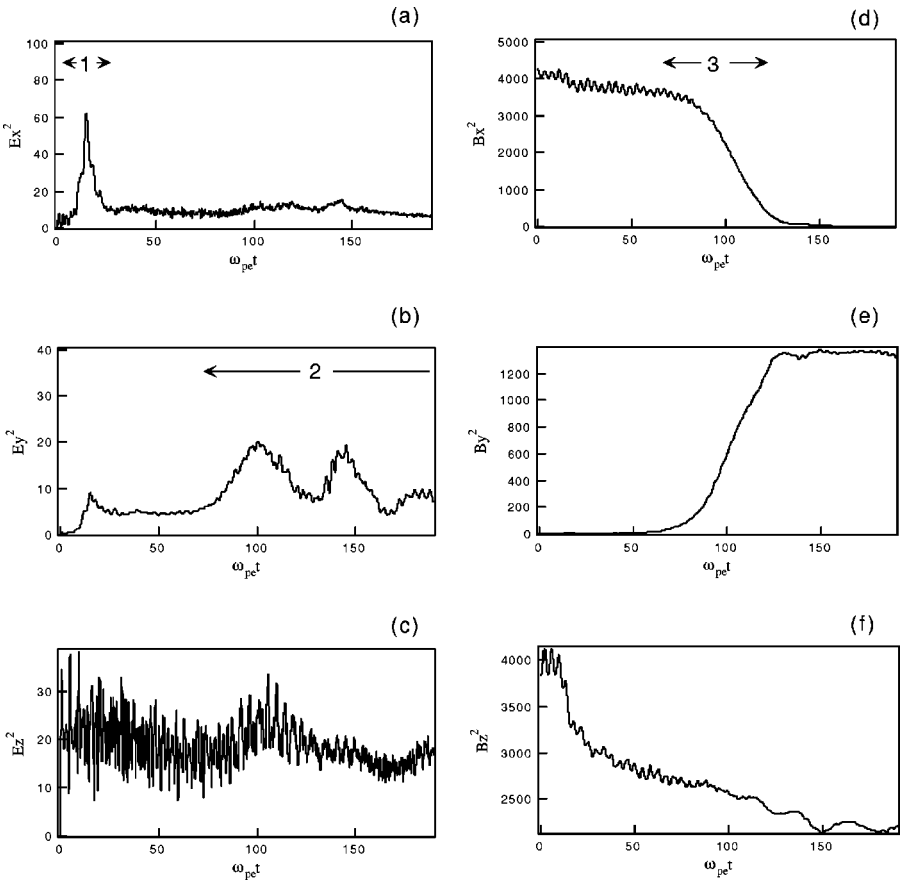

FIG. 1. The time history of the electric field energies (a) $\int\int E_x^2 dx\,dy$, (b) $\int\int E_y^2 dx\,dy$, and (c) $\int\int E_x^2 dx\,dy$ and the magnetic field energies (d) $\int\int B_x^2 dx\,dy$, (e) $\int\int B_y^2 dx\,dy$, (f) $\int\int B_z^2 dx\,dy$. Three different phases are shown by (1) current-driven Buneman instability phase in (a), (2) trapping phase in (b), and (3) magnetic reconnection phase in (d).

quency $\omega_{pe}=\sqrt{e^2 n/\epsilon_0 m_e}$ ($\epsilon_0=1$) to the electron cyclotron frequency $\omega_e=eB_0/m_e$, $\omega_{ce}/\omega_{pe}=1.47$ for maximum magnetic field strength B_0, the ratio of the electron thermal velocity parallel to the magnetic field B_x to the light velocity $v_{te}/c=\sqrt{2\kappa T_e/m_e}/c=0.094$; the Debye length $\lambda_{De}=0.89\Delta$; the skin depth $c/\omega_{pe}=9.6\Delta$; the plasma beta value $\beta=0.002$; and the temperature of electrons T_e to the temperature of positrons T_p, $T_e/T_p=1$. The gyroradius for both thermal electrons and positrons is $\rho_e=\rho_p=0.47\Delta$ for maximum magnetic field strength B_0.

III. SIMULATION RESULTS

In this section we show our simulation results. The time development during the simulation period is divided into three phases: (1) phase of the current-driven Buneman instability [7], (2) particle trapping phase, and (3) magnetic reconnection phase. As shown in Fig. 1, these three phases are characterized in the time history of the electric field energy of the system, $\int\int E_x^2 dx\,dy$, $\int\int E_y^2 dx\,dy$, and the magnetic field energy of the system, $\int\int B_x^2 dx\,dy$. In Fig. 2 we present the time development of magnetic field vectors (B_x vs B_y) in the *x*-*y* plane and the magnetic field intensity B_z with gray scale. As seen in these figures, the configuration with the force-free magnetic field becomes unstable. Subsequently it breaks into current filaments and eventually the system changes structurally with strong dissipation of magnetic field energy. We discuss in detail the three physical processes in the following subsections.

A. Phase of the current-driven Buneman instability

As seen in Fig. 1(a), there appears strong enhancement of the electric field energy $\int\int E_x^2 dx\,dy$ in the early stage of the simulation. We call this stage a phase of the current-driven Buneman instability. Because the particle drift velocity to sustain the force-free magnetic field given by Eqs. (2.1)–(2.3) exceeds the thermal velocity, there occurs the Buneman instability in both the *x* and *z* directions. As the present model of the simulation is uniform in the *z* direction, the instability appears only in the *x* direction. The drift velocity in the *x* direction is localized near $y=20$ and $y=60$, therefore the current-driven Buneman instability in pair plasmas (see Sturrock [8], p. 111) occurs near both the above regions. Figure 3(a) shows the spacial distribution of the electric field E_x at $\omega_{pe}t=1.5$ associated with the Buneman instability. We can calculate the growth rate of the instability from the time history of the electric field energy $\int\int E_x^2 dx\,dy$ in Fig. 3(b) as $\gamma/\omega_{pe}=0.53$, which is in good agreement with the theoretical value of 0.5 (see Sturrock [8], p. 112). While the wavelength of the instability to give the maximum growth rate is

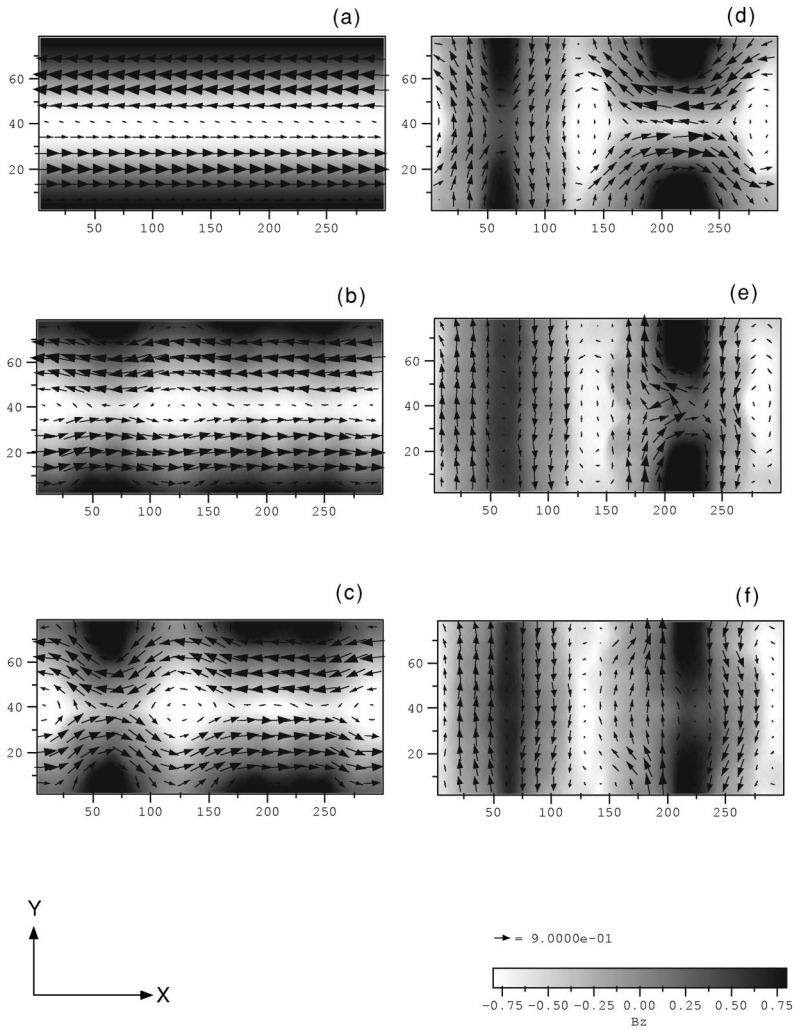

FIG. 2. Time development of the magnetic field vector $(B_x - B_y)$ and B_z with gray scale: (a) $\omega_{pe}t=0$, (b) $\omega_{pe}t=75$, (c) $\omega_{pe}t=90$, (d) $\omega_{pe}t=105$, (e) $\omega_{pe}t=120$, and (f) $\omega_{pe}t=135$.

also compared with the theory, $kc/\omega_{pe}=(\frac{3}{2})^{1/2}c/v_d \approx 5.0$, which also gives a good agreement.

The electrostatic waves excited by the current-driven Buneman instability could scatter the current-carrying particles in the *x*-*y* plane and act as the collisionless anomalous resistivity through the wave-particle interaction. Therefore, there appears a decay of magnetic field energy $\int\int B_x^2 dx\,dy$ as seen in Fig. 1(f), which also coincides with a decay of the electric field energy $\int\int E_x^2 dx\,dy$ as seen in Fig. 1(a). But the electric field energy remains for a long time after the decay. We note here that the inductive electric field E_y due to the change of the magnetic field B_z also remains after the decay of the instability. These electric fields may contribute to the second phase of the particle trapping.

Here we note that if the particle drift velocity to sustain the force-free magnetic field given by Eqs. (2.1)–(2.3) does not exceed the thermal velocity $(v_d=0.76v_{te})$, there occurs no Buneman instability. Figure 4 presents the time development of the electric field energies $(\int\int E_x^2 dx\,dy,\ \int\int E_y^2 dx\,dy)$ and magnetic field energies $(\int\int B_x^2 dx\,dy,\ \int\int B_y^2 dx\,dy)$, showing that nothing happens during the simulation period.

B. Particle trapping phase

In this subsection we discuss the phase after the current-driven Buneman instability, especially focusing on the development of the electric field in the *x*-*y* plane. As seen in Fig. 5(a), the electric fields randomly distributed in the *x*-*y* plane after the first instability phase begin to reorganize [see Fig. 5(b)] and grow as seen in the time history of the electric field energy $\int\int E_y^2 dx\,dy$ in Fig. 1(b). This restructuring of the electric fields is associated with particle trapping in the two-dimensional electric field as seen in Fig. 6, where the electron distribution in the *x*-*y* plane is shown at $\omega_{pe}t=105$. In this figure only a fraction 0.01 of all the electrons is plotted.

We find that some electrons are confined and trapped near the weak electric field. The trapping effect is also seen in Fig. 7, which shows the phase space plots $(v_x - x)$ and $(v_y - y)$ at $\omega_{pe}t=105$. As seen in Fig. 1(b), the quasiperiodic slow oscillation of the electric field energy $\int\int E_y^2 dx\,dy$ appears from about $\omega_{pe}t=75$. This oscillation may be caused by particle trapping in the electric field. The trapping of particles by the electric field is localized near the null region of the magnetic field B_x, therefore, the current-carrying par-

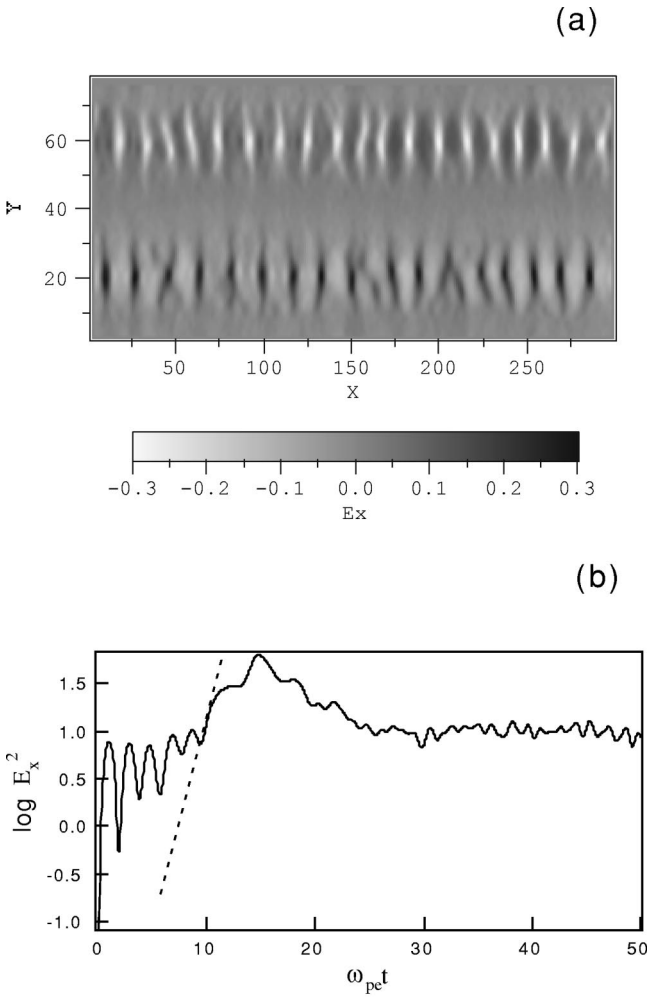

FIG. 3. (a) The spatial distribution of the electric field E_x at $\omega_{pe}t=15$. (b) The time history of $\int\int E_x^2 dx\, dy$, where the observed growth rate is calculated from a dotted line in the figure.

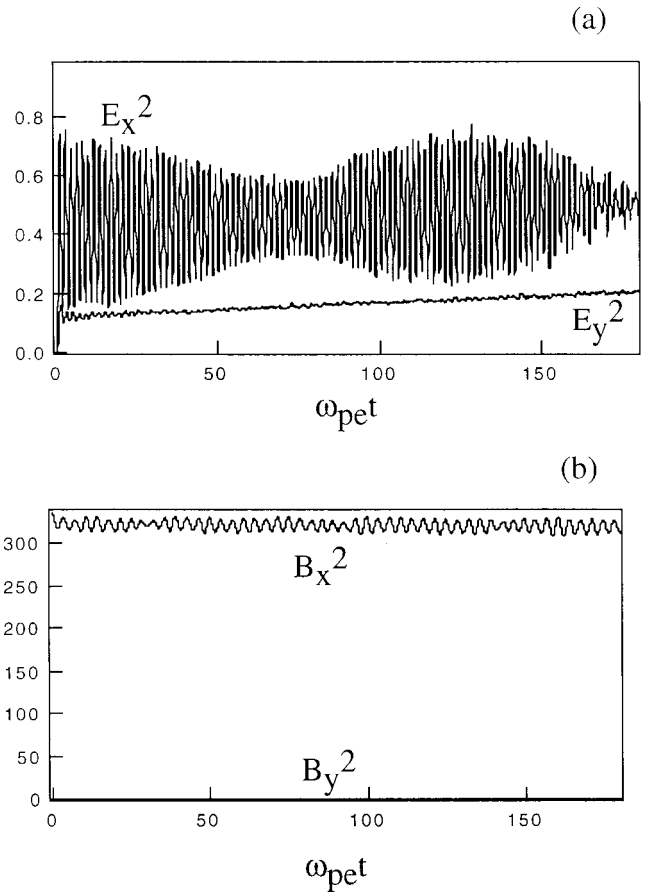

FIG. 4. (a) The time history of $\int\int E_x^2 dx\, dy$ and $\int\int E_y^2 dx\, dy$, (b) the time history of $\int\int B_x^2 dx\, dy$ and $\int\int B_y^2 dx\, dy$ when there occurs no Buneman instability.

ticles in the z direction could be dragged by this trapping effect. Eventually the magnetic field (B_x) dissipation due to the collisionless anomalous resistivity can be triggered as seen in Fig. 1(d).

C. Magnetic reconnection phase

As discussed in the previous subsection, the magnetic reconnection starts to occur at around $\omega_{pe}t=75$ as seen in Fig. 2(b), which time coincides with the restructuring of the electric fields in the x-y plane as seen in Fig. 4(b). The magnetic reconnection begins from the region where plasma pinching is relatively weak around $x=60$ as seen in Fig. 2(c), then, more strong reconnection could be triggered around $x=225$ at $\omega_{pe}t=120$ as seen in Fig. 2(e). As seen in Fig. 2(f), there appear four current sheets along the y direction after the magnetic reconnection; in that period, 43% of the initial magnetic field can dissipate to heat background plasma as well as high-energy particles.

In Fig. 8 both electron and positron velocity distribution functions are shown. The solid curves show the initial distributions, while the dotted curves show the velocity distributions at $\omega_{pe}t=180$. The final three velocity distributions show almost isotropic heating, because particles are mainly heated parallel to the magnetic field, as they are initially strongly magnetized. Figure 9 shows the electron energy spectrum, which shows an exponential type with two temperatures.

Finally we note that when the drift velocity of the initial current that makes the force-free magnetic field becomes as weak as half of the previous simulation case, we observed the almost same result as the previous case, except that the excited electric field energy becomes less weak. Therefore, the production of high-energy particles also becomes weak. While the drift velocity becomes more larger than the previous case, the magnetic reconnection tends to start more quickly after the Buneman instability saturates.

D. Effect of mass ratio

We investigate here the effect of the mass ratio between electrons and protons on the subsequent physical processes presented in the previous subsections. We did several simulations by changing the mass ratio from $m_p/m_e=100$ to 1836, keeping $v_d=0.25c=2.65v_{te}$. In the following we show the simulation results for the case of the mass ratio $m_p/m_e=1836$.

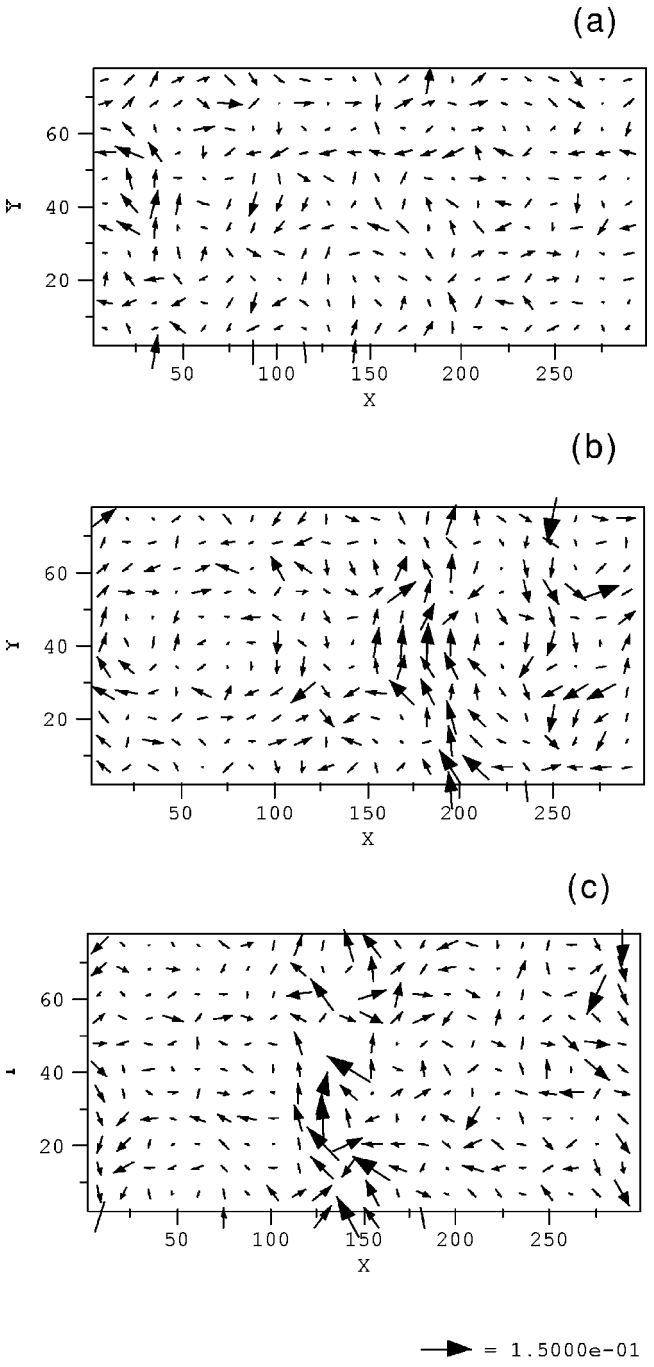

FIG. 5. The electric field vector plots in the *x*-*y* plane at (a) $\omega_{pe}t=75$, (b) $\omega_{pe}t=105$, and (c) $\omega_{pe}t=135$.

Figure 10 shows the time development of the electric field energies ($\int\int E_x^2 dx\,dy$, $\int\int E_y^2 dx\,dy$) and magnetic field energies ($\int\int B_x^2 dx\,dy$, $\int\int B_y^2 dx\,dy$). The main difference from the pair plasma is due to the fact that the initial Buneman instability starts to grow slowly due to the finite mass ratio: the growth rate is proportional to $(m_e/m_p)^{2/3}$. As seen in Fig. 10(a), the electric field E_x grows slowly with a linear growth rate predicted by the theory [7] and saturates at around $\omega_{pe}t=140$. After the Buneman instability saturates, the magnetic reconnection begins to develop with the decrease of magnetic field energy ($\int\int B_x^2 dx\,dy$) as seen in Fig. 10(b). Figure 11 shows the time evolution of the vector plots of the magnetic fields and the B_z component with gray scale. As the anomalous resistivity is much weaker for heavy protons, the B_z component does not change significantly. The overall time development of magnetic fields in the electron-proton plasmas is quite similar to the pair plasma, except for the behavior of the electron trapping phase.

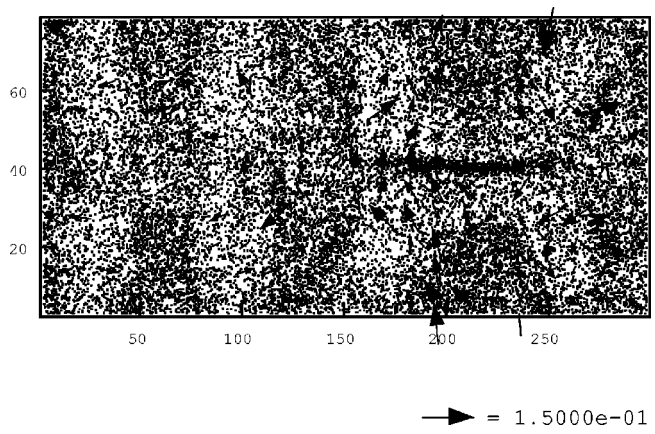

FIG. 6. The electron distribution in the *x*-*y* plane overlapped with the electric field vector plot at $\omega_{pe}t=105$.

Figure 12 shows the snapshots of the electric field E_y and the charge density distribution at $\omega_{pe}t=400$ at which time, it corresponds to the triggering phase of the magnetic reconnection, corresponding to Fig. 11(d). As seen in Fig. 12(b), the electron trapping is mostly associated with large sheetlike structures in the *x* direction as well as the small sheetlike structures associated with the Buneman instability. This spacial structures are more complicated as compared with the pair plasma, as seen in Fig. 6.

IV. SUMMARY

It has been shown by using a two-dimensional, fully relativistic, electromagnetic particle-in-cell simulation code that a force-free magnetic configuration in collisionless, electron-positron (pair) plasmas becomes unstable against current-driven Buneman instability and subsequently there occurs a strong magnetic field energy dissipation associated with collisionless magnetic reconnection. The collisionless magnetic reconnection can be driven by particle trapping due to two-dimensional electric potentials remaining in the nonlinear stage of the current-driven Buneman instability. About 43% of the initial magnetic field energy dissipates and is transformed to plasma heating as well as high-energy particle production. The energy spectrum in the high-energy region is given by an exponential type with two temperatures. We also investigated the effect of the mass ratio between electrons and protons on the subsequent physical processes by changing the mass ratio from $m_p/m_e=100$ to 1836. We found that the overall time development in the electron-proton plasmas is quite similar to the pair plasma case, except for the behavior of the electron trapping phase.

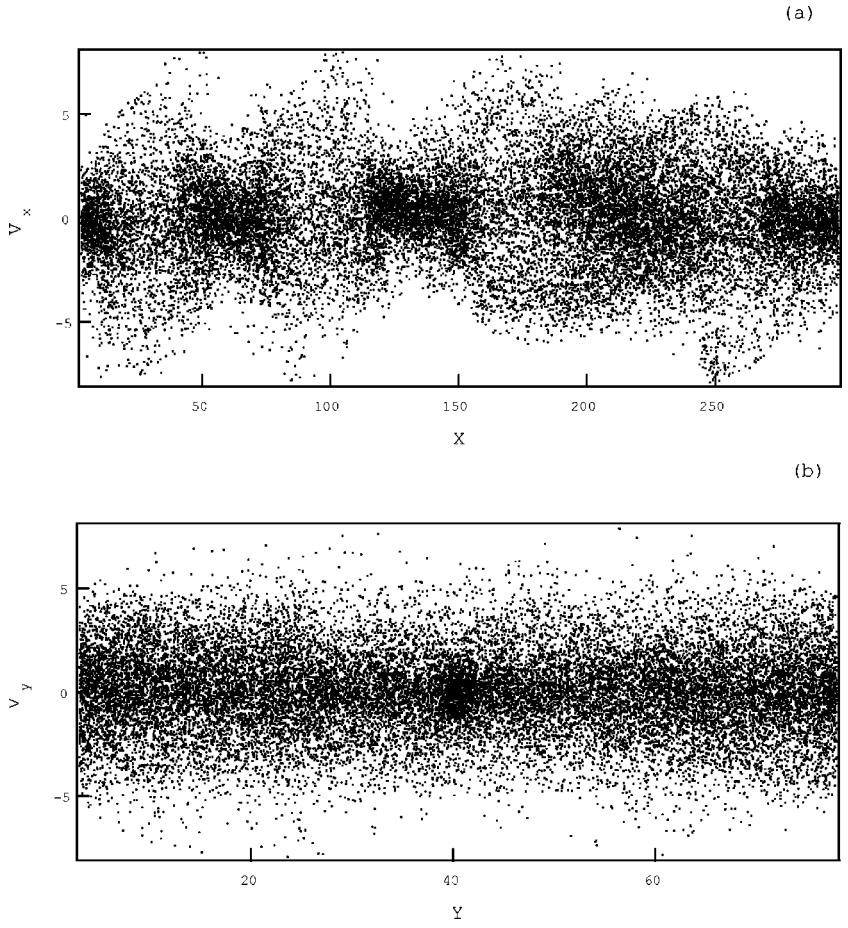

FIG. 7. The phase space plots of the electrons at $\omega_{pe}t=105$: (a) v_x-x and (b) v_y-y.

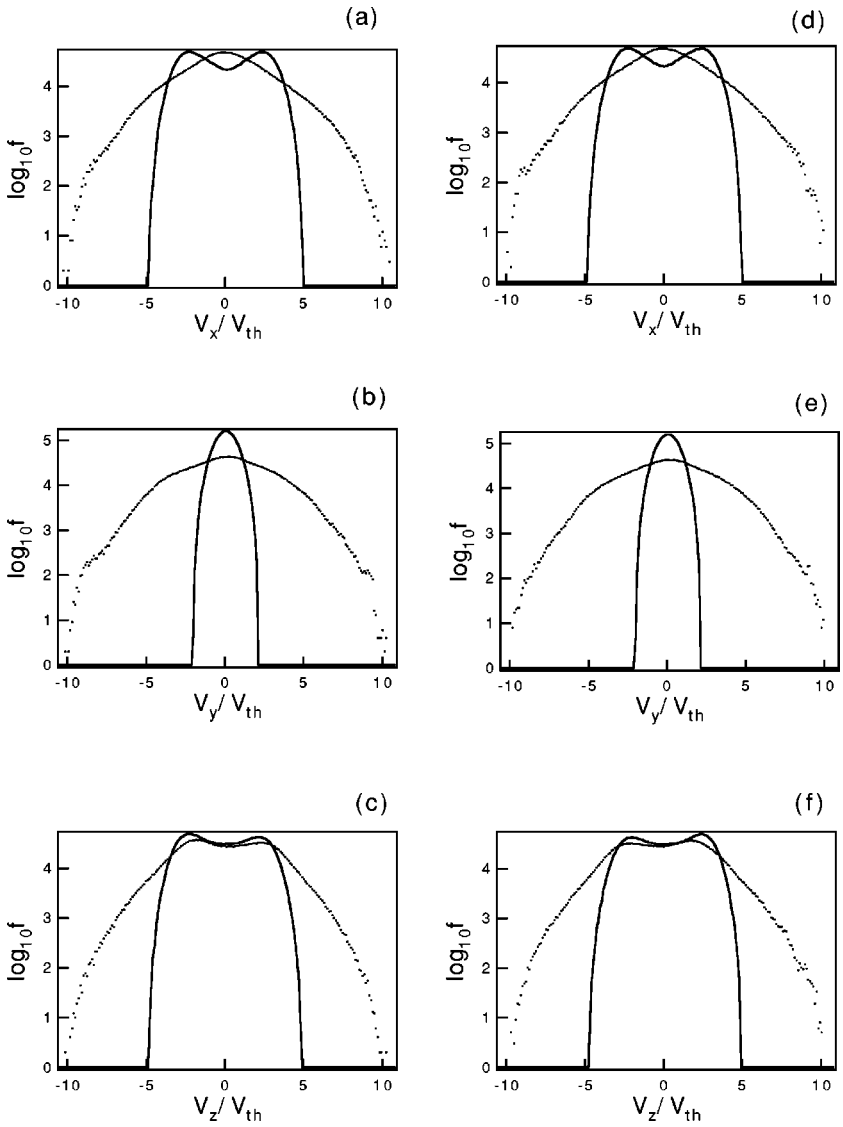

FIG. 8. The electron distribution functions (a)–(c) and positron distribution functions (d)–(f) at $\omega_{pe}t=0$ (solid line) and $\omega_{pe}t=180$ (dotted line).

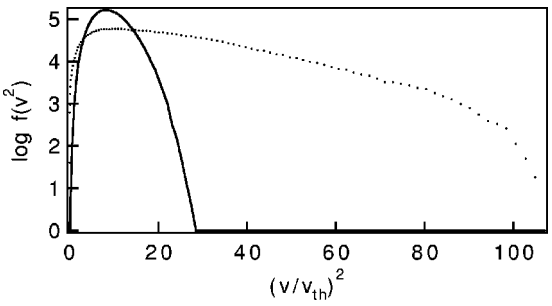

FIG. 9. The electron energy spectrum at $\omega_{pe}t=0$ (solid line) and $\omega_{pe}t=180$ (dotted line), where $v^2=v_x^2+v_y^2+v_z^2$.

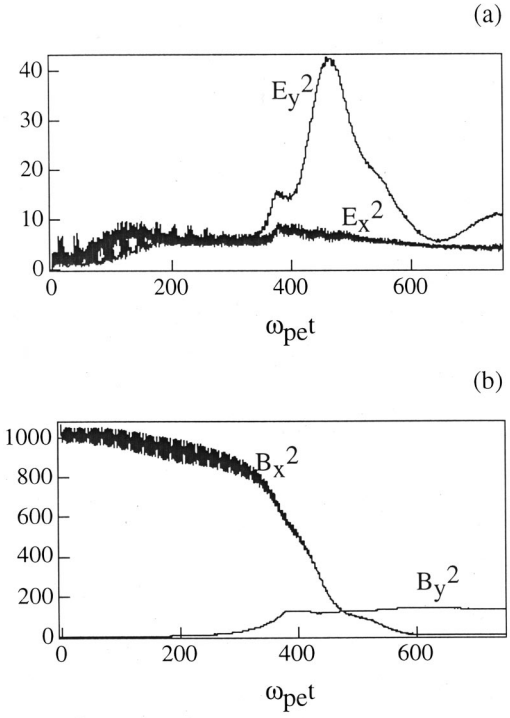

FIG. 10. (a) The time history of $\int\int E_x^2 dx\, dy$ and $\int\int E_y^2 dx\, dy$, (b) the time history of $\int\int B_x^2 dx\, dy$ and $\int\int B_y^2 dx\, dy$ for the electron-proton plasma.

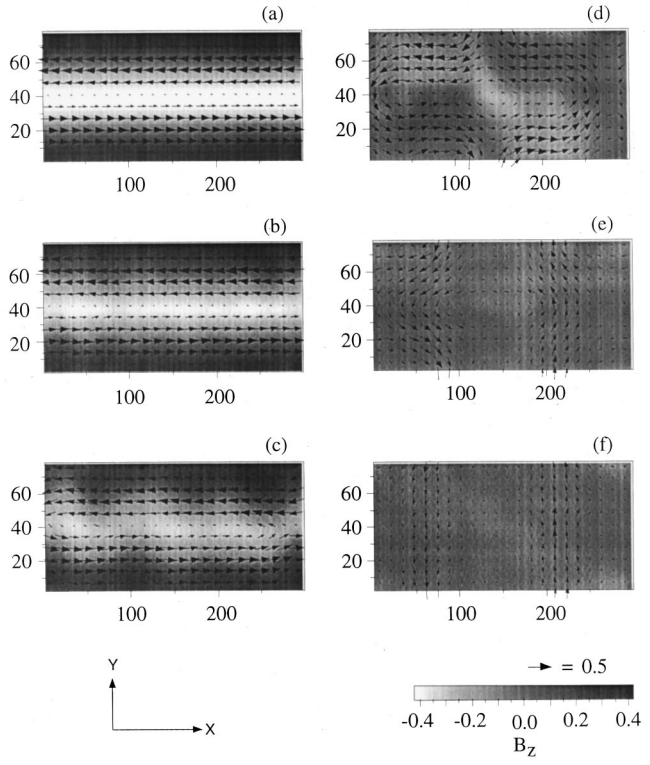

FIG. 11. Time development of the magnetic field vector ($B_x - B_y$) and B_z with gray scale for the electron-proton plasma: (a) $\omega_{pe}t=0$, (b) $\omega_{pe}t=200$, (c) $\omega_{pe}t=300$, (d) $\omega_{pe}t=400$, (e) $\omega_{pe}t=500$, and (f) $\omega_{pe}t=600$.

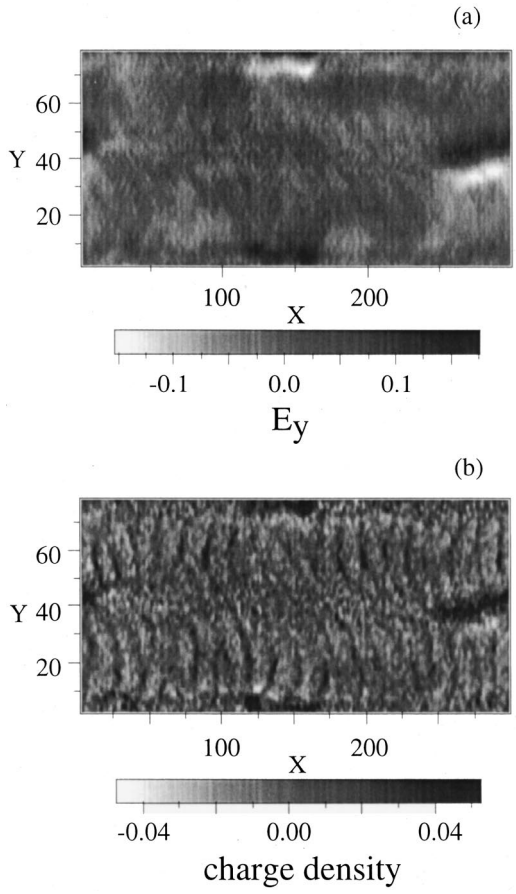

FIG. 12. (a) The electric field E_y and (b) the charge density at $\omega_{pe}t=400$ for the electron-proton plasma.

ACKNOWLEDGMENT

This work was supported by a Grand-in-Aid for Scientific Research from the Japanese Ministry of Education (11695028).

[1] J. W. Dungey, Phys. Rev. Lett. **6**, 47 (1961); P. A. Sweet, Proc. IAU Symp. **6**, 123 (1958); E. N. Parker, J. Geophys. Res. **79**, 1558 (1957); H. E. Petschek, in *Physics of Solar Flares* edited by W. N. Hess, AAS-NASA Symposia Proceedings No. SP-50 (NASA, Washington, DC, 1964), p. 425; V. M. Vasyliunas, Rev. Geophys. **13**, 303 (1975); D. Biskamp, *Nonlinear Magnet Hydrodynamics* (Cambridge University Press, Cambridge, 1993), Chap. 6; J. I. Sakai and C. de Jager, Space Sci. Rev. **77**, 1 (1996).

[2] G. Laval, R. Pellat, and M. Vullemin, Plasma Phys. Controlled Nucl. Fusion Res. **2**, 259 (1966); A. A. Galeev, in *Basic Plasma Physics*, edited by M. N. Rosenbluth and R. Z. Sagdeev (North-Holland, Amsterdam, 1984), Vol. 2, Chap. 6.2, p. 314.

[3] D. Winske, Phys. Fluids **24**, 1069 (1981).

[4] M. Ozaki, T. Sato, R. Horiuchi, and C. S. Group, Phys. Plasmas **3**, 2265 (1996); Z. Zhu and R. M. Winglee, J. Geophys. Res. **101**, 4885 (1996); P. L. Pritchett and F. V. Coroniti, J. Geomagn. Geoelectr. **48**, 833 (1996); G. Lapenta and J. U. Brackbill, J. Geophys. Res. **102**, 27 099 (1997); W. Daughton, Phys. Plasmas **6**, 1329 (1999); R. Horiuchi and T. Sato, National Institute for Fusion Science Report No. 600 (unpublished).

[5] J. I. Sakai, D. Sugiyama, N. Bobrova, and S. V. Bulanov, in *Proceedings of the Conference on Magnetic Reconnection, Tokyo, 2000*, edited by M. Hoshino, R. L. Stenzel, and K. Shibata (Earth, Planets and Space, Terra Scientific Publishing Company, Tokyo, 2001).

[6] O. Buneman, in *Computer Space Plasma Physics, Simulation Techniques and Software*, edited by H. Matsumoto and Y. Omura (Terra Scientific, Tokyo, 1993), p. 67.

[7] O. Buneman, Phys. Rev. **115**, 503 (1959).

[8] P. A. Sturrock, *Plasma Physics* (Cambridge University Press, Cambridge, 1994).